CRYSTAL GROWTH & DESIGN

Article

Cite This: *Cryst. Growth Des.* 2020, 20, 906−915

pubs.acs.org/crystal

Selective Synthesis of a Salt and a Cocrystal of the Ethionamide−Salicylic Acid System

Davide Bernasconi,[†] Simone Bordignon,[†] Federica Rossi,[†] Emanuele Priola,[†] Carlo Nervi,[†] Roberto Gobetto,[†] Dario Voinovich,[‡] Dritan Hasa,[‡] Nghia Tuan Duong,[§] Yusuke Nishiyama,[§,∥] and Michele R. Chierotti*[,†]

[†]Department of Chemistry and NIS Centre, University of Torino, Via Giuria 7, 10125 Torino, Italy

[‡]Department of Chemical and Pharmaceutical Sciences, University of Trieste, Piazzale Europa 1/Via L. Giorgieri 1, 34127 Trieste, Italy

[§]NMR Science and Development Division, RIKEN SPring-8 Center, and Nano-Crystallography Unit, RIKEN-JEOL Collaboration Center, Yokohama, Kanagawa 230-0045, Japan

[∥]JEOL Resonance Inc., 3-1-2 Musashino, Akishima, Tokyo 196-8558, Japan

Supporting Information

ABSTRACT: Herein is presented a rare example of salt/cocrystal polymorphism involving the adduct between ethionamide (ETH) and salicylic acid (SAL). Both the salt and cocrystal forms have the same stoichiometry and composition and are both stable at room temperature. The synthetic procedure was successfully optimized in order to selectively obtain both polymorphs. The two adducts' structures were thoroughly investigated by means of single-crystal X-ray diffraction, solid-state NMR spectroscopy, and density functional theory (DFT) calculations. From the solid-state NMR point of view, the combination of mono- and multinuclear experiments (^{1}H MAS, ^{13}C and ^{15}N CPMAS, ^{1}H-{^{14}N} D-HMQC, ^{1}H−^{14}N PM-S-RESPDOR) provided undoubted spectroscopic evidence about the different positions of the hydrogen atom along the main N···H···O interaction. In particular, the ^{1}H−^{14}N PM-S-RESPDOR allowed N−H distance measurements through the ^{1}H detected signal at a very high spinning speed (70 kHz), which remarkably agree with those derived by DFT optimized X-ray diffraction, even on a natural abundance real system. The thermodynamic relationship between the salt and the cocrystal was inquired from the experimental and computational points of view, enabling the characterization of the two polymorphs as enantiotropically related. The performances of the two forms in terms of dissolution rate are comparable to each other but significantly higher with respect to the pure ETH.

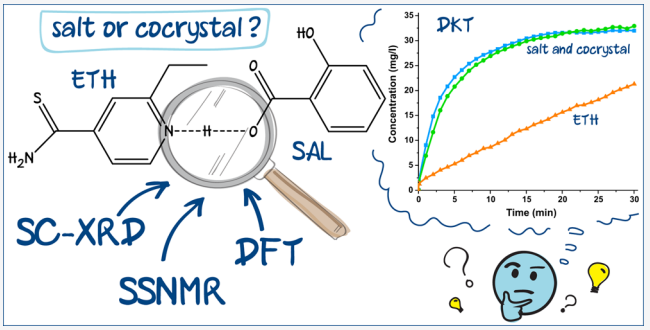

INTRODUCTION

Crystal engineering has established itself as a valuable tool in the design of functional molecular solids. In particular, tuning physicochemical properties of a crystalline material by changing the arrangement of its components, on the basis of their molecular shapes and functional groups, is of outmost importance in the pharmaceutical industry.[1−3] Indeed, the solubility, stability, bioavailability, and manufacturability of an active pharmaceutical ingredient (API) can be properly modified using different solid forms, such as polymorphs, cocrystals, and salts.[4−6] In particular, the latter two are examples of multicomponent systems, namely, formed by the API and a second GRAS ("generally recognized as safe") molecule, that are neutral in the case of cocrystals or ionic in the case of salts. The distinction between these two types of crystalline forms is crucial for pharmaceutical companies, not only because they are often characterized by different physicochemical and pharmacokinetic performances but also from the legal and regulatory point of view, connected to intellectual property issues.[7−9] Furthermore, it is also important under an academic perspective, related to the study of structure−property relationships, molecular recognition mechanisms, and weak interactions.[9−13] In fact, in many cases, the main distinction between salts and cocrystals depends on whether a complete proton transfer has occurred or not along the axis of a hydrogen bond (HB) interaction between the API and the molecular partner.[14] This will generate ionized species in the former case and neutral ones in the latter. Usually, a specific pair of molecules produces either a salt or a cocrystal, although the neutral or ionic character of the adduct can be modulated by temperature or stoichiometry.[15,16] However, to the best of our knowledge, there are only

Received: October 1, 2019
Revised: December 16, 2019
Published: December 16, 2019

DOI: 10.1021/acs.cgd.9b01299
Cryst. Growth Des. 2020, 20, 906−915

four examples in the literature in which the same chemical species can crystallize both as a cocrystal and a salt with the same composition and stoichiometry and at the same temperature: tartaric acid−β-alanine,[17] sulfamethazine−saccharin,[18] isonicotinamide−citric acid,[19] and dinitrobenzoic acid−haloanilines.[20] Only for the first three, the authors managed to obtain the salt or cocrystal on purpose, while for the fourth the achievement remained stochastic.

Here we present the ethionamide (ETH)−salicylic acid (SAL) system, for which we managed to selectively drive the synthesis toward both the salt (ETH^+SAL^-) and the cocrystal (ETH·SAL) forms. ETH (Scheme 1, left) is an important

Scheme 1. Chemical Structures of Ethionamide (ETH) and Salicylic Acid (SAL), with Atom Numbering

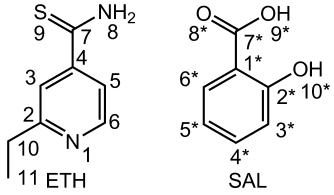

antitubercular drug, included in the Essential Medicine List by the World Health Organization. Tuberculosis still represents one of the most dangerous infective diseases, and new therapies have continuously been investigated.[21] ETH is an analogue of isoniazid, and it is employed specifically for the treatment of multidrug resistant tuberculosis (MDR-TB).[22,23] Due to its limited water solubility (0.84 mg/mL),[24] and consequent unfavorable bioavailability, ETH has been extensively investigated and a series of cocrystals and salts, both organic and inorganic, have been reported.[25−28] We selected SAL (Scheme 1, right) as a coformer since ETH bears a pyridine moiety and the pyridine−carboxylic acid heterosynthon is one of the most robust and reliable available synthons.[29,30] Furthermore, SAL is a GRAS phenolic acid with analgesic and anti-inflammatory properties.[31,32]

In order to fully identify and characterize the structural features of the two polymorphs, a complementary powder and single-crystal X-ray diffraction (PXRD and SC-XRD, respectively) and solid-state NMR (SSNMR) approach, supported by DFT calculations, was employed. From the SSNMR point of view, both common and advanced techniques (^{1}H MAS, ^{13}C and ^{15}N CPMAS, ^{1}H-{^{14}N} J- and D-HMQC, ^{1}H−^{14}N PM-S-RESPDOR) were applied to discriminate between the neutral or ionic nature of the adducts. In particular, the ^{1}H−^{14}N PM-S-RESPDOR is a new sequence,[33,34] which allows one to determine ^{1}H−^{14}N distances through the ^{1}H detected signal at a very high spinning speed (70 kHz), and here it was tested on a natural abundance real system.

The relative stability of the two polymorphs was assessed by calorimetric analyses (DSC and TGA), competitive slurry experiment, and DFT calculations, while inquiry of their solubility properties was conducted by dissolution kinetic tests (DKTs).

EXPERIMENTAL SECTION

SAL (purity > 99%) and all used solvents were purchased from Sigma-Aldrich, while ETH (purity > 98%) was purchased from Alfa Aesar. All reagents were used as received, without purification.

For ETH^+SAL^-, the bulk powder was achieved by kneading 50 mg (0.3 mmol) of ETH and 42 mg (0.3 mmol) of SAL with a few drops of MeOH for 20 min. Crystals suitable for SC-XRD were obtained through seeding crystallization at room temperature of 5 mL of an *i*PrOH−MeOH (1:3) solution using the bulk powder as seed.

For ETH·SAL, the bulk powder was prepared by employing a rotavapor for rapid evaporation of 30 mL of a MeOH solution containing 50 mg (0.3 mmol) of ETH and 42 mg (0.3 mmol) of SAL. Single crystals were obtained by evaporation of a MeOH solution at room temperature (5 mL).

For competitive slurry experiment, a mixture of 40 mg of ETH·SAL and 40 mg of ETH^+SAL^- was stirred with a few milliliters of MeOH. After 48 h, the resulting sample was filtered and analyzed by FTIR-ATR (see Supporting Information Figure S17).

FTIR-ATR. FTIR-ATR spectra were collected on a Fourier transform Equinox 55 (Bruker) spectrophotometer equipped with an ATR device; the resolution was set at 2 cm^{-1} for all spectra. A spectral range of 400−3800 cm^{-1} was scanned, using KBr as a beam splitter. All spectra were acquired with 16 scans.

X-ray Diffraction. Single crystals of ETH·SAL and ETH^+SAL^- were analyzed with a Gemini R Ultra diffractometer operating at 293(2) K, using a Mo Kα source (λ = 0.71073 Å). Data collection and reduction were performed using the CrysAlisPro software.[35] The crystal structures were solved by direct methods and refined with the full matrix least-squares technique on F2 using the SHELXS-97 and SHELXL-97 programs.[36,37] All non-hydrogen atoms were refined anisotropically; hydrogen atoms bonded to unambiguous sites were placed in geometrical positions and refined using the riding model. Hydrogen atoms between pyridinic nitrogen and carboxylic oxygen sites of nearby molecules were detected in the Fourier maps, and their positions were checked through SSNMR. See Table 1 for the crystallographic data of ETH^+SAL^- and ETH·SAL, and Tables S1a−S4a and S1b−S4b in the Supporting Information for more details, i.e., bond distances and angles (refer to Scheme 1 in the main text for the atom numbering). The powder diffractogram of ETH was obtained

Table 1. Crystallographic Data of ETH^+SAL^- and ETH·SAL

	ETH^+SAL^-	ETH·SAL
empirical formula	$C_{15}H_{16}N_2O_3S$	$C_{15}H_{16}N_2O_3S$
FW	304.36	304.36
temp/K	295	295
cryst syst	monoclinic	monoclinic
space group	$P2_1/c$	$P2_1/n$
a/Å	13.6128(14)	12.931(6)
b/Å	7.1563(9)	4.3009(14)
c/Å	16.3031(19)	28.040(7)
α/deg	90	90
β/deg	107.078(12)	92.65(4)
γ/deg	90	90
vol/Å^3	1518.2(3)	1557.7(10)
Z	4	4
ρ_{calc}/(g/cm^3)	1.332	1.298
μ/mm^{-1}	0.224	0.219
cryst size/mm^3	0.34 × 0.22 × 0.21	0.35 × 0.34 × 0.22
radiation	Mo Kα (λ = 0.71073)	Mo Kα (λ = 0.71073)
2θ range for data collection/deg	6.498−50.04	6.824−50.044
reflns collected	6564	6087
indepen reflns	2687 [R_{int} = 0.0510; R_σ = 0.0674]	2742 [R_{int} = 0.0373; R_σ = 0.0484]
data/restraints/params	2687/0/201	2742/0/203
goodness-of-fit on F^2	1.030	1.028
final *R* indexes [$I \geq 2\sigma(I)$]	R_1 = 0.0571, R_{w2} = 0.1068	R_1 = 0.0522, R_{w2} = 0.1219
final *R* indexes (all data)	R_1 = 0.1118, R_{w2} = 0.1313	R_1 = 0.0909, R_{w2} = 0.1451
largest diff peak/hole/(e Å^{-3})	0.15/−0.17	0.17/−0.17

DOI: 10.1021/acs.cgd.9b01299
Cryst. Growth Des. 2020, 20, 906−915

on the same Gemini R Ultra diffractometer, equipped with an X-ray source using Cu Kα radiation (λ = 1.54 Å). Data were collected and processed through the CrysAlisPro software. The powder patterns of SAL, ETH·SAL, and ETH$^+$SAL$^-$ were obtained on a Philips X'Pert PW3020 Bragg–Brentano instrument, equipped with an X-ray source using Cu Kα radiation (λ = 1.54506 Å) operating at 40 kV and 30 mA. Measurements were carried out in $\theta/2\theta$ mode, with a scanning range of 5–40° for 2θ.

SSNMR Measurements. All SSNMR measurements were recorded at room temperature on a solid-state NMR spectrometer (JNM-ECZ600R) at a magnetic field of 14.1 T, equipped with 3.2 or 1 mm ^{1}H/X double-resonance probes, operating at ^{1}H, ^{13}C, ^{15}N, and ^{14}N Larmor frequencies of 600.1, 150.9, 60.8, and 43.4 MHz, respectively. For 2D ^{1}H-{^{14}N} D-HMQC and PM-S-RESPDOR experiments, ETH·SAL and ETH$^+$SAL$^-$ were separately packed into 1 mm zirconia rotors and spun at a MAS frequency of 70 kHz. The ^{1}H radio frequency (rf) field for $\pi/2$ and π pulses was 208 kHz for ETH$^+$SAL$^-$ and 278 kHz for ETH·SAL,while it was 140 kHz for the $SR4^2_1$ recoupling sequence for both samples. For D-HMQC experiments, the ^{14}N pulse length was 8 μs and the highest technically possible rf power on ^{14}N was used. The mixing time (τ) and recycling delay were (171 μs; 20 s) and (342 μs; 25 s) for ETH$^+$SAL$^-$ and ETH·SAL, respectively. The two-dimensional ^{1}H-{^{14}N} D-HMQC spectra were recorded with 24 scans, 32–42 t_1 points, and rotor-synchronized t_1 increment of 14.3 μs. The dummy scans were 8 and 4 for ETH$^+$SAL$^-$ and ETH·SAL, respectively. The states-TPPI method was employed for the quadrature detection along the indirect dimension. The experimental times were 11.2 h for ETH$^+$SAL$^-$ and 10.7 h for ETH·SAL. For PM-S-RESPDOR experiments (performed at JEOL Resonance Inc.), the length of the PM pulse was $10t_R$ (0.14 ms) and the ^{14}N rf field was 80 kHz (calibrated through NH_4Cl) for both samples. In order for the experiments to reach the steady state, prior to the PM-S-RESPDOR measurements, 32 or 54 dummy scans were applied on ETH$^+$SAL$^-$ and ETH·SAL samples, respectively. The mixing time (τ) was varied from 0 to 1.0 ms for ETH$^+$SAL$^-$ and from 0 to 1.5 ms for ETH·SAL. The number of scans and recycling delays were (32, 75 s) for ETH$^+$SAL$^-$ and (36, 72 s) for ETH·SAL. The total experimental times were 26 and 40 h for ETH$^+$SAL$^-$ and ETH·SAL, respectively. ^{1}H MAS spectra were performed at 70 kHz with an echo pulse sequence (90°–τ–180°–τ) to remove the probe background (^{1}H 90° pulse = 0.77 μs; three transients for all samples). 1D ^{13}C CPMAS and ^{15}N CPMAS measurements were performed on cylindrical 3.2 mm o.d. zirconia rotors with a sample volume of 60 μL spun at 20 (^{13}C) and 12 kHz (^{15}N). All experiments employed the ramped CP pulse sequence with a ^{1}H 90° pulse of 3.8 μs, a contact time in the range of 3.5–4.5 ms, a number of scans in the range 325–1150 for ^{13}C spectra and 1253–13000 for ^{15}N spectra, and a recycle delay ranging between 4.2 and 12.5 s, depending on the sample. The two-pulse phase modulation (TPPM) ^{1}H decoupling scheme[38] was used for ^{13}C, while SPINAL64[39] was employed for ^{15}N, both with a rf field of 119 kHz. ^{1}H, ^{13}C, ^{14}N, and ^{15}N chemical shift scales were referenced through the resonances of adamantane (^{1}H signal at 1.87 ppm), glycine (^{13}C methylene signal at 43.5 ppm), $(NH_4)_2SO_4$ (^{14}N signal at 0 ppm,and ^{15}N signal at 24.6 ppm with respect to NH_3), respectively, which were used as external standards.

DFT Calculations. Periodic lattice calculations were performed with Quantum Espresso version 6.4.1,[40,41] adopting the nonlocal vdW-DF2 method,[42−48] choosing the b86r functional of Hamada.[49] Geometry optimizations were performed starting from the solid-state crystal structures, with a full geometry optimization with cell relaxation. The relaxed cells are in substantial agreement with experimental data, with volumes smaller than 4.6% and 4.8% for the salt and the cocrystal, respectively. The PBE PAW pseudopotentials from the PS Library 1.0.0[50] were adopted, with a cutoff of 60 Ry. The Brillouin zones were automatically sampled with the Monkhorst–Pack scheme[51] in an approach similar to that previously described.[52] Geometry optimizations were performed with grid meshes of 1 × 3 × 1 and 1 × 2 × 1 for ETH·SAL and ETH$^+$SAL$^-$, respectively. The energy difference between ETH$^+$SAL$^-$ and ETH·SAL, in Rydberg, was divided by 8, the number of molecules in the cell (i.e., Z) and then converted into kJ/mol. Magnetic shieldings were calculated using the GIPAW method,[53] with a cutoff energy of 80 Ry. The theoretical absolute ^{13}C magnetic shielding (σ) values were converted into the corresponding chemical shifts (δ) using the following conversion: $\delta_{calc} = \sigma_{ref} - \sigma$. Here, σ_{ref} is the reference shielding, obtained by plotting the experimental chemical shifts δ_{expt} against the GIPAW-calculated chemical shieldings (σ). A linear regression model with slope constrained to (−1) was applied to find the best fit to the data. The value of σ_{ref} is determined by the intercept with the y axis.[54,55] The obtained values are 167.13 and 165.86 ppm for the salt and cocrystal, respectively (see Figure S1).

Thermal Analyses. TGA measurements were performed over a temperature range of 35–350 °C under a 50 mL·min^{-1} N_2 flow, on a Q600 SDT TA Instruments equipped with a DSC heat flow analyzer. Samples (5–10 mg of weight) were placed into the furnace inside alumina crucibles and heated with a ramp of 10 °C·min^{-1}. DSC curves were collected on a DSC Q200 TA Instrument. Samples were accurately weighed (5–10 mg) and put into sealed aluminum pans. Calibration for temperature and heat flow was performed using high purity standards of n-decane, benzene, and indium. All measurements were performed in a 40–130 °C temperature range, with heating rates of 10 °C·min^{-1}.

Dissolution Kinetic Tests. DKTs were carried out in phosphate buffer (pH = 7.4). For each measurement, an equivalent amount of solid to give 4 mg of ETH was added to 100 mL of the thermostatically controlled (at 37 °C) dissolution medium. Each test lasted 60 min. The solution was kept homogeneous by continued stirring at 100 rpm, and concentrations were measured using an optical fiber system (HELLMA, Milan, Italy) linked to a spectrophotometer (ZEISS, Germany). UV measurements were performed at the maximum absorption wavelength of ETH, namely, 288 nm. A calibration curve (Figure S2) was obtained with five diluted ETH solutions in phosphate buffer (the concentrations used were the following: 8, 10, 16, 20, and 40 mg/L), while pure phosphate buffer was used as blank.

RESULTS AND DISCUSSION

Both the salt (ETH$^+$SAL$^-$) and the cocrystal (ETH·SAL) forms of the ETH-SAL system were selectively obtained. The salt was achieved by manual liquid-assisted grinding (LAG), employing methanol, acetonitrile, dichloromethane, or n-pentane as solvent. However, this easiness of formation in the solid state was not reflected in solution, since many crystallization trials at room temperature using a variety of polar and apolar solvents failed in giving the compound (see Table 2). On the contrary, at first the cocrystal stochastically appeared while trying to crystallize the salt with methanol,

Table 2. List of the Different Solvents Employed in the Two Preparation Methods, Liquid-Assisted Grinding (LAG) and Solution Crystallization (SOL), and of the Corresponding Products[a]

solvent	product (LAG)	product (SOL)
methanol	salt	SM + cocrystal
ethanol	salt	SM + cocrystal
dichloromethane	salt	SM + cocrystal
acetonitrile	salt	SM
n-penthane	salt	
isopropanol		SM
chloroform		SM
tetrahydrofurane		SM
diethyl ether		SM

[a]All SOL trials were conducted at room temperature. The products were analyzed by FTIR-ATR (data not shown). SM stands for starting materials.

DOI: 10.1021/acs.cgd.9b01299
Cryst. Growth Des. 2020, 20, 906–915

Table 3. Cruz-Cabeza Model Applied on Examples of Salt−Cocrystal Polymorphism. (P_{obs} = Observed Probability)

adduct	ΔpK_a[a]	$P_{obs}(AB)$/%	$P_{obs}(A^-B^+)$/%	expected product
ethionamide−salicylic acid	2[b]	38	62	salt or cocrystal
tartaric acid−β-alanine	0.63[c,d]	61.3	38.7	salt or cocrystal
sulfamethazine−saccharin	0.8[18]	58.4	41.6	salt or cocrystal
isonicotinamide−citric acid	0.4[e]	65.2	34.8	salt or cocrystal
3,5-dinitrobenzoic acid−4-iodoaniline	0.99[19]	55.2	44.8	salt or cocrystal
3,5-dinitrobenzoic acid−4-bromoaniline	1.07[19]	53.8	46.2	salt or cocrystal
3,5-dinitrobenzoic acid−4-iodo-2-methylaniline	0.84[19]	57.7	42.3	salt or cocrystal
3,5-dinitrobenzoic acid−4-bromo-2-methylaniline	0.89[19]	56.9	43.1	salt or cocrystal

[a] ΔpK_a = pK_a(protonated base) − pK_a(acid). [b] pK_a(ethionamide) = 5.0;[24] pK_a(salicylic acid) = 3.[31] [c] pK_a(β-alanine) = 3.63;[76] pK_a(tartaric acid) = 3.0.[77] [d] For β-alanine, the selected pK_a value is relative to the carboxylic group. In fact, a careful analysis of the reported structures indicates that, in the salt, the transferred proton is shared between the carboxylate moieties of two zwitterionic β-alanine molecules. [e] pK_a(isonicotinamide) = 3.45[78] (calculated); pK_a(citric acid) = 3.05[78] (calculated).

ethanol, or dichloromethane as solvents (see Table 2). To obtain the pure bulk powder, rapid evaporation of a methanol solution by means of a rotary evaporator was employed.[56] The large supersaturation generated this way ensured quantitative precipitation of ETH·SAL. A competitive slurry experiment in methanol at room temperature (see Figure S3 for the FTIR-ATR spectra) confirmed that the salt is the thermodynamic phase while the cocrystal is a kinetic product in these conditions (see Thermal Analyses for further discussion). Therefore, this system seems to follow the Oswald rule of stages,[57,58] which states that the less stable form tends to crystallize first. It is also worth noting that the proton transfer is not influenced by the character of the solvent, i.e., polar/apolar or protic/aprotic. Actually, it is the method itself, promoting either the kinetic or thermodynamic form, that seems to determine the position of the hydrogen atom along the main N···H···O interaction. Although simple grinding is often employed to obtain thermodynamic polymorphs,[59−61] LAG can generate different polymorphs upon changing the solvent.[62,63] In this case, however, all trials led to the same thermodynamically stable polymorph.[64]

The outcome of the reaction between an acid and a base has been historically proposed to be predictable, at least to a certain degree, by employing the so-called "pK_a rule". Such rule states that the larger the difference between the pK_a values of the two components, the greater the chance to obtain a salt (vice versa, cocrystal is favored).[65−67] According to a model suggested by Cruz-Cabeza et al.,[66] for $-1 < \Delta pK_a < 4$ the probability of cocrystal or salt formation can be quantitatively computed using the following formula: $P_{obs}(AB)/\% = -17\Delta pK_a + 72$ and $P_{obs}(A^-B^+)/\% = 17\Delta pK_a + 28$, respectively. As shown in Table 3, the ETH-SAL system well fits in the pK_a model, which calculates an almost equal chance of salt and cocrystal formation. For the sake of comparison, the same model was applied to the other examples of salt/cocrystal polymorphism. It is apparent that all of the reported systems fall in the region of uncertain prediction, with ΔpK_a values around 1. This is somewhat expected, since in this region there is not a clear predominance of either salt or cocrystal formation, meaning that both forms are theoretically obtainable. Although the reported samples are not statistically relevant, satisfying the pK_a rule seems necessary to achieve salt/cocrystal polymorphism. However, it is worth keeping in mind that it is the crystalline environment as a whole that plays a decisive role in defining the hydrogen position along an HB at room temperature, as proposed by Childs and co-workers.[67]

The appearance of the new crystalline forms was confirmed by different techniques, namely, FTIR-ATR (Figure S4 in the Supporting Information), PXRD (Figures S5 and S6), and solid-state NMR (SSNMR) (see below). The ionic or neutral character of the products was investigated by SC-XRD, supported by ^{15}N CPMAS, ^{1}H-{^{14}N} D-HMQC, and N−H distances measurements by $^{14}N-^{1}H$ PM-S-RESPDOR SSNMR experiments, which account for very accurate $^{1}H-^{14}N$ distance values on natural abundance samples.[33,34] For both forms, the comparison of the experimental and calculated PXRD patterns (Figures S5 and S6) indicates that the single-crystal structures are representative of the bulk powders.

Crystal Structure Analysis. Yellow block-shaped crystals of ETH^+SAL^-, suitable for SC-XRD, were obtained by crystallization from an iPrOH−MeOH (1:3) solution with the addition of a seed of the ground powder. It crystallizes in a monoclinic $P2_1/c$ space group (see Table S1a in the Supporting Information) with one ETH cation and one SAL anion in the asymmetric unit (Figure 1, top). The S1 sulfur is disordered over two positions. The main intermolecular interaction is the predicted charge-assisted heterosynthon O9*···H−N1 (O9*···N1 = 2.592(4) Å), as shown by the similar C−O distances of the carboxylate moiety (C7*−O8* = 1.234(4) Å and C7*−O9* = 1.278(3) Å), and the $^{14}N-^{1}H$ distance by PM-S-RESPDOR SSNMR analysis (see below). These distances are consistent with a proton transfer to the ETH pyridinic nitrogen. A weaker HB is also observed between the ETH thioamidic group as donor and a carboxylate of a second SAL anion as acceptor (O8*···N8 = 2.868(4) Å). This secondary HB interaction involving the SAL carboxylate, which is absent in the cocrystal (see below), helps in favoring the proton transfer and in stabilizing the charged species.[68] The analysis of the crystal packing (Figure 1, middle) highlights the presence of $R_4^4(22)$, tetrameric rings, formed by pairs of ETH^+SAL^- units, and a contribution from π−π stacking interactions (Figure 1, bottom) between contiguous rings (intercentroid distances, 3.615(4) and 3.588(4) Å).

On the other hand, ETH·SAL, whose crystals were obtained by crystallization from a MeOH solution, crystallizes in a monoclinic $P2_1/n$ space group. The asymmetric unit (Figure 2, top) contains one ETH and one SAL molecule. The ETH ethyl group shows disorder over two positions. The main interaction still corresponds to the aforementioned O···N heterosynthon, no longer charge-assisted (O9*···N1 = 2.646(4) Å) as shown by the larger difference between C−O distances of the carboxylic moiety (C7*−O9* = 1.303(4) Å

DOI: 10.1021/acs.cgd.9b01299
Cryst. Growth Des. 2020, 20, 906−915

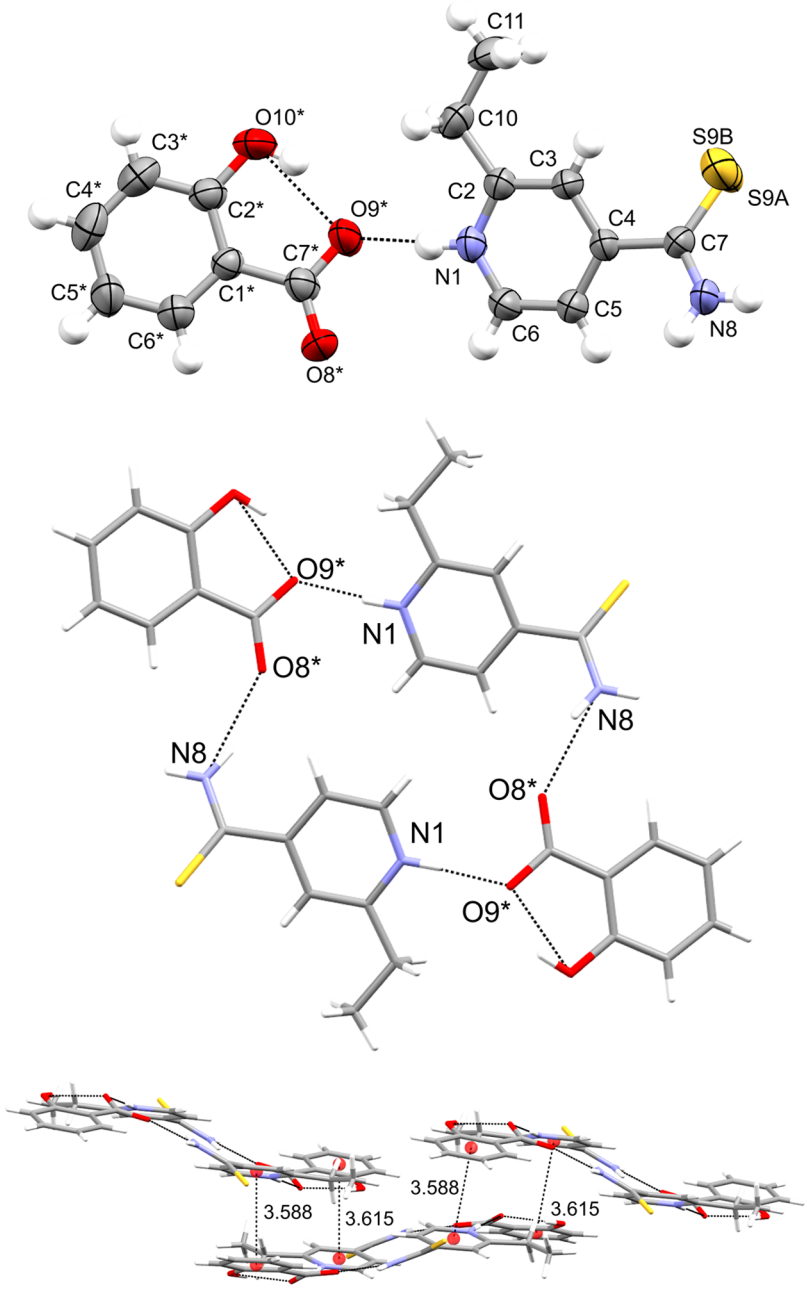

Figure 1. Asymmetric unit of ETH^+SAL^- represented by ellipsoids at 50% of probability, highlighting the main heterosynthon and the sulfur atom disorder (top). Details of the tetrameric rings (middle) and the $\pi-\pi$ stacking interactions (the disorder is removed for clarity) (middle and bottom).

and C7*−O8* = 1.222(4) Å) and confirmed by the $^{14}N-^{1}H$ distances measured by SSNMR (see below). These pieces of evidence clearly indicate that, in this case, the proton transfer does not occur. A further weaker HB involves the ETH thioamidic group as donor and a hydroxyl oxygen of a second SAL molecule as acceptor (O10*···N8 = 2.919(4) Å). The tetrameric rings are substituted by spiral-shaped structures (Figure 2, middle and bottom), due to the torsion of the thioamidic moiety with respect to the ETH ring (C3−C4−C7−N8 dihedral angle = −132°).

Solid-State NMR Characterization. A complete SSNMR characterization (^{1}H MAS, ^{13}C and ^{15}N CPMAS spectra, 2D ^{1}H-{^{14}N} D-HMQC spectra and $^{14}N-^{1}H$ PM-S-RESPDOR experiments) was performed. All chemical shifts are listed in Table S5, while the ^{1}H MAS and ^{13}C CPMAS spectra are reported in Figures S7 and S8 in the Supporting Information. The main evidence of the ionic/neutral nature of the compounds is provided by ^{15}N CPMAS spectra (Figure 3). Indeed, pyridinic ^{15}N chemical shift is recognized in being particularly sensitive to its protonation state. For ETH^+SAL^-, the N1 signal exhibits a marked shift of almost 100 ppm toward lower frequencies (from 309.0 ppm for pure ETH down to 211.9 ppm), consistent with a complete proton transfer to the pyridinic nitrogen. For ETH·SAL, the low-frequency shift is much less pronounced (from 309.0 to 273.4 ppm), indicating the formation of a neutral HB.[69]

This qualitative analysis is further expanded by 2D ^{1}H-{^{14}N} D-HMQC spectra (Figure 4), which allow for the ^{1}H

DOI: 10.1021/acs.cgd.9b01299
Cryst. Growth Des. 2020, 20, 906−915

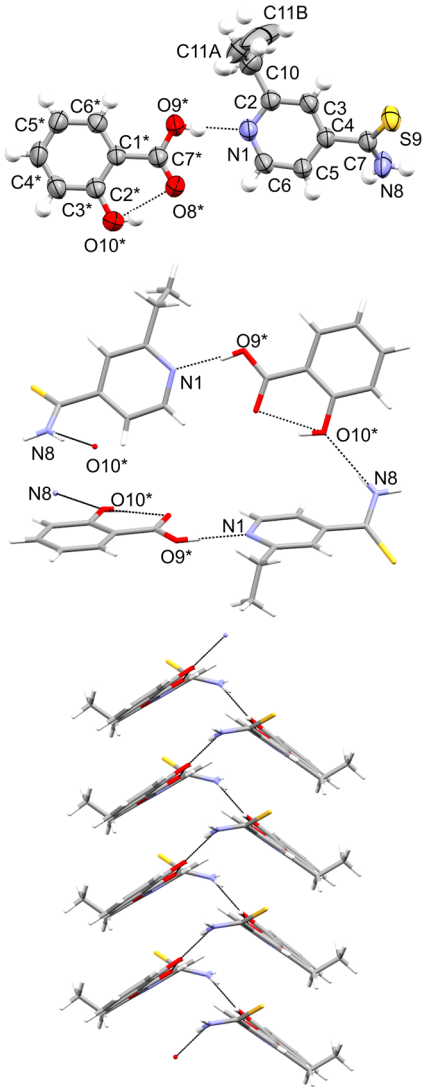

Figure 2. Asymmetric unit of ETH·SAL represented by ellipsoids at 50% of probability, highlighting the main heterosynthon and the ethyl group disorder (top). Details of the packing and of the spiral-shaped structures (the disorder is removed for clarity) (middle and bottom).

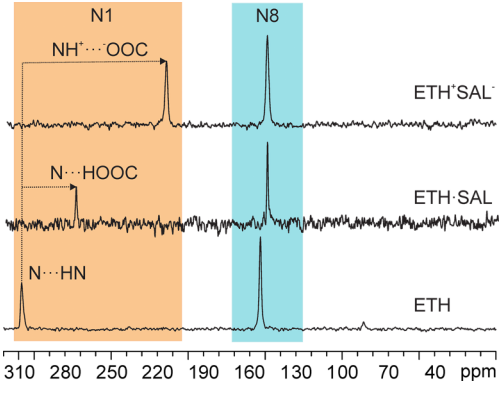

Figure 3. ^{15}N (60.8 MHz) CPMAS spectra of ETH·SAL, ETH$^+$SAL$^-$, and pure ETH with assignments, recorded at 12 kHz at room temperature. The pyridinic nitrogen (N1) shift is highlighted, to mark the different chemical shifts in the two polymorphs, with respect to pure ETH.

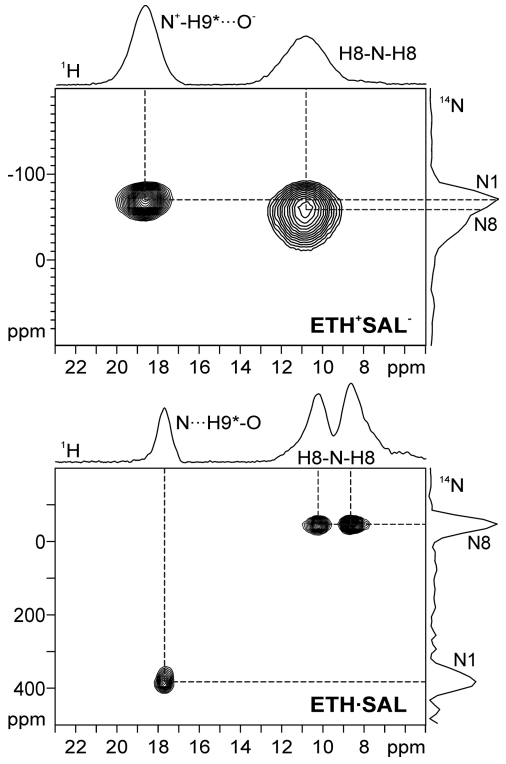

Figure 4. 2D ^{1}H-{^{14}N} D-HMQC spectra (^{1}H, 600.1 MHz; ^{14}N, 43.4 MHz; ν_R = 70 kHz) of ETH$^+$SAL$^-$ (top) and ETH·SAL (bottom).

assignment of the thioamidic N−H (H8) and pyridinic N$^+$−H or N···H (H9*) resonances as follows: at 10.8 (H8) and 18.4 ppm (H9*) for ETH$^+$SAL$^-$ and at 10.3/8.7 (H8) and 17.3 ppm (H9*) for ETH·SAL (see Supporting Information for further discussion).

Finally, the N−H distances were measured by ^{14}N−^{1}H PM-S-RESPDOR SSNMR experiments, which provide very accurate ^{1}H−^{14}N distances, leveraging the ^{1}H detected signal at a very high spinning speed (70 kHz). Details of the experimental setup of the pulse sequence are given elsewhere.[33,34] In short, the method based on the PM-S-RESPDOR sequence requires the acquisition of two sets of data to extract the distance information. First, the experiment is run without irradiation on the ^{14}N channel, resulting in the ^{1}H signal $S_0(\tau)$. Second, the same experiment is run with the ^{14}N PM pulse which prevents the refocusing of the ^{1}H−^{14}N heteronuclear dipolar coupling, leading to the ^{1}H signal $S'(\tau)$. The PM-S-RESPDOR fraction curves are obtained by plotting $\Delta S/S_0 = (S_o(\tau) - S'(\tau))/S_o(\tau))$ as a function of mixing time, τ. These fraction curves are then matched by analytical curves where the dipolar coupling between ^{1}H and ^{14}N ($b^{1}_{\mathrm{H}-^{14}\mathrm{N}}/(2\pi)$) is the only fitting parameter. Once experimental and analytical curves match, the extracted dipolar coupling ($b^{1}_{\mathrm{H}-^{14}\mathrm{N}}/(2\pi)$) is used in the following equation to obtain accurate ^{1}H−^{14}N distances:

$$^{1}\mathrm{H}-^{14}\mathrm{N}\ \text{distance/Å} = \left(\frac{120.1}{b^{1}_{\mathrm{H}-^{14}\mathrm{N}}/(2\pi/\mathrm{kHz})}\frac{\gamma_{^{14}\mathrm{N}}}{\gamma_{^{1}\mathrm{H}}}\right)^{1/3}$$

where γ_X (X = ^{1}H or ^{14}N) represents the gyromagnetic ratio of the X nucleus.

Herein, the N−H distances are extracted by matching the experimental and analytical fitting of $\Delta S/S_0$ fraction curves of

DOI: 10.1021/acs.cgd.9b01299
Cryst. Growth Des. 2020, 20, 906−915

the ^{1}H signals of H9* at 18.4 ($ETH^{+}SAL^{-}$) and 17.3 ppm (ETH·SAL), as assigned from the 2D ^{1}H-{^{14}N} D-HMQC spectra. The extracted values were obtained by considering mixing time (τ) values up to 0.4 and 1.0 ms for $ETH^{+}SAL^{-}$ and ETH·SAL, respectively. The experimental and simulated $\Delta S/S_0$ fraction curves are represented in Figure 5 as black dots

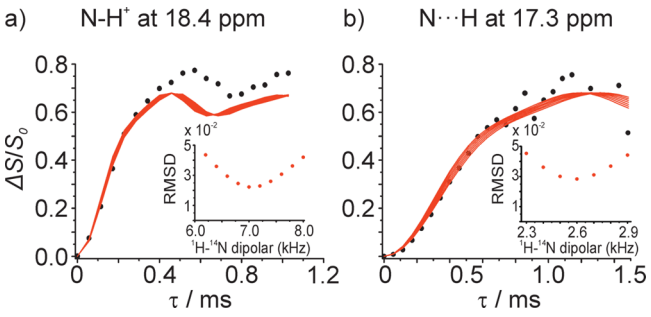

Figure 5. Experimental ^{14}N−^{1}H $\Delta S/S_0$ fraction curves (black dots) achieved by PM-S-RESPDOR of (a) $ETH^{+}SAL^{-}$ and (b) ETH·SAL at ^{1}H chemical shifts of 18.4 and 17.3 ppm, respectively, and analytical fitting curves (red solid lines). The insets show the best fitting ^{1}H−^{14}N dipolar coupling on the basis of root-mean-square deviation analysis.

and solid red lines, respectively. The best fittings are obtained with N−H distances of 1.07 Å for $ETH^{+}SAL^{-}$ and of 1.50 Å for ETH·SAL. The same analysis was also carried out for the NH_2 group (^{1}H peaks at 10.8 and 10.3 ppm for $ETH^{+}SAL^{-}$ and ETH·SAL, respectively) for which the $\Delta S/S_0$ fraction curves are reported in Figure S9, together with the obtained N−H distances. These NMR distance values perfectly agree with the reference mean values (1.128 Å for the salts; 1.491 Å for the cocrystals) extrapolated from a CSD survey (CSD version 5.40, updated in September 2019 on the N−H and N−D distances of pyridine−carboxylic acid interactions in neutron structures; see Figure S10 in the Supporting Information for the 29 found structures).

DFT Calculations. We employed DFT-D nonlocal vdW-df2-b86r method with a fully relaxed cell in order to optimize the single-crystal structures (see Figures S11 and S12 for superpositions). Our objective was 3-fold: (i) to support chemical shift assignments by calculating chemical shieldings and shifts; (ii) to obtain reference values for the N−H distances and compare them to the SSNMR extrapolated ones; (iii) to investigate the two polymorphs' relative stability by computing their lattice energy difference. The reliability of the optimized structures is provided by the calculated chemical shifts, which show agreement with the experimental ones, displaying RMS values (for ^{13}C) of 2.09, for the salt and 1.46, for the cocrystal. The optimized N−H distances display values of 1.087 and 1.488 Å for N^{+}−H and N···H, respectively (see Table 4), which again demonstrate the remarkable accuracy of the PM-RESPDOR experiments. Finally, the DFT-D calculations indicate that the salt form has a lower lattice energy of 4.95 kJ/mol per molecule with respect the cocrystal. This result, along with the higher density of the salt (salt = 1.332 g/cm^{-3}; cocrystal = 1.298 g/cm^{-3}) confirms the stability relationship derived by the competitive slurry and thermal analysis (see below).

Table 4. Comparison among N−H Distances Values from Neutron Diffraction Structures (Mean Values), NMR, and DFT Data

	neutron diffraction/Å	SSNMR/Å	DFT-D/Å
$ETH^{+}SAL^{-}$	1.128	1.07	1.087
ETH·SAL	1.491	1.50	1.488

Thermal Analysis. A DSC run up to 130 °C was conducted on the samples. As shown in Figure S13, both forms display a melting point around 104 °C, while the salt presents an additional broad endothermic event around 99 °C due to salt−cocrystal polymorphic conversion. Indeed, the FTIR-ATR spectrum of the salt sample after heating to 100 °C matches the cocrystal one (Figure S14). Thus, the two phases are enantiotropically related,[70] with the salt being the most stable one at room temperature. The cocrystal is kinetically stable, as no reverse transitions are observed on cooling. If compared to the melting point of pure ETH (around 165 °C), it is apparent that the new adducts lead to a lower thermal stability, as do almost all ETH multicomponent forms reported in the literature.[24−27] The TGA experiments do not show weight loss before 150 °C, confirming that both adducts are free from solvents (Figure S15).

Dissolution Kinetic Tests. DKTs were carried out in water (pH 7.4 phosphate buffer) at 37 °C for both forms, to evaluate the dissolution rate with respect to pure ETH (Figure 6). As expected, pure ETH exhibits a slow dissolution rate. On

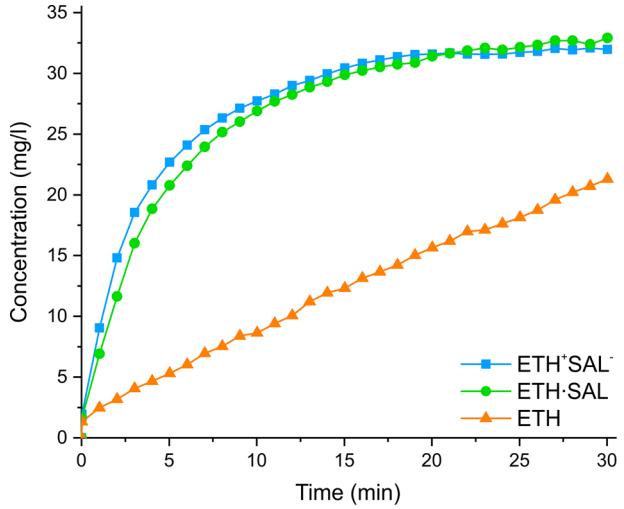

Figure 6. Dissolution profiles of (blue) $ETH^{+}SAL^{-}$ and (green) ETH·SAL, with respect to pure (orange) ETH. DKT were carried out in water (pH 7.4 phosphate buffer) at 37 °C.

the other hand, both salt and cocrystal display a pronounced improvement, providing an ETH concentration of 32 mg/L, which is reached in 24 min, while the concentration of pure ETH after the same time is about 22 mg/L. Interestingly, both $ETH^{+}SAL^{-}$ and ETH·SAL show almost identical dissolution profiles; i.e., the protonation state does not affect the overall in vitro dissolution properties in agreement with previous findings.[67] A number of works have questioned the widespread belief that pharmaceutical salts are more soluble than cocrystals.[71−74] All of these articles are based on systems made by different components, i.e., one API and a series of coformers, while our adducts are formed by the same components, thus offering a decisive support to their claims. Indeed, the complexity of the solubilization process cannot be restricted to the position of a hydrogen along a single HB.

DOI: 10.1021/acs.cgd.9b01299
Cryst. Growth Des. 2020, 20, 906−915

In addition, more generally, a similar dissolution performance does not necessarily mean that other physicochemical properties are the same. In fact, several examples showed that cocrystals and salts display different properties. For instance, Sandhu et al.[75] reported that the hygroscopicity of a solid can be significantly reduced through cocrystallization. Additionally, in a structural analysis of over 80 cocrystals and salts, Aakeröy et al.[12] indicated that the frequency of solvate formation among the salt forms was 19%, while such frequency reduced to 5% in the case of cocrystals. While analyzing several physicochemical properties such as hygroscopicity of $ETH^{+}SAL^{-}$ and ETH·SAL would be interesting for comparison purposes, this type of information is beyond the scope of the present study.

CONCLUSIONS

In conclusion, the ethionamide−salicylic acid system is a rare example of salt/cocrystal polymorphism. The two forms have the same stoichiometry and composition and are both stable at room temperature, with the salt being the thermodynamic phase and the cocrystal being the kinetic one. We managed to optimize the synthetic procedure to selectively obtain both forms. Thus, the method itself, promoting either the kinetic or thermodynamic form, seems to determine the position of the hydrogen atom along the main N···H···O interaction, rather than the character of the solvent (protic/aprotic or polar/apolar). We have unraveled the different ionic and neutral character of the two polymorphs, by a combined X-ray diffraction and SSNMR approach by leveraging the impressive robustness of the PM-RESPDOR sequence for $^{1}H-^{14}N$ distance measurements. Their thermodynamic relationship was investigated from the experimental and computational points of view, enabling one to characterize the two polymorphs as enantiotropically related. The performances of the two forms in terms of dissolution rate are comparable to each other and significantly higher with respect to the pure ETH. This is further evidence that packing, HBs, ionic or neutral character, and dispersion forces are intimately connected in determining the macroscopic properties of molecular crystals and should not be considered independently.

ASSOCIATED CONTENT

Supporting Information

The Supporting Information is available free of charge at https://pubs.acs.org/doi/10.1021/acs.cgd.9b01299.

Additional crystallographic data, PXRD patterns, FTIR-ATR whole spectra, additional SSNMR data and spectra, DSC and TGA graphs, along with further discussion (PDF)

Accession Codes

CCDC 1936640 and 1958233 contain the supplementary crystallographic data for this paper. These data can be obtained free of charge via www.ccdc.cam.ac.uk/data_request/cif, or by emailing data_request@ccdc.cam.ac.uk, or by contacting The Cambridge Crystallographic Data Centre, 12 Union Road, Cambridge CB2 1EZ, UK; fax: +44 1223 336033.

AUTHOR INFORMATION

Corresponding Author

*E-mail: michele.chierotti@unito.it.

ORCID

Carlo Nervi: 0000-0002-3712-7369
Roberto Gobetto: 0000-0002-2431-8051
Dritan Hasa: 0000-0003-2147-9121
Yusuke Nishiyama: 0000-0001-7136-1127
Michele R. Chierotti: 0000-0002-8734-6009

Notes

The authors declare no competing financial interest.

ACKNOWLEDGMENTS

Elena Amadio is acknowledged for the drawing in the abstract and Table of Contents. D.B. thanks Simone Benivento for useful suggestions. F.R. thanks GIDRM and the Annalaura Segre's family for the scholarship "GIDRM/Borse Annalaura Segre".

REFERENCES

(1) Cerreia Vioglio, P.; Chierotti, M. R.; Gobetto, R. Pharmaceutical Aspects of Salt and Cocrystal Forms of APIs and Characterization Challenges. *Adv. Drug Delivery Rev.* **2017**, *117*, 86−110.
(2) Kavanagh, O. N.; Croker, D. M.; Walker, G. M.; Zaworotko, M. J. Pharmaceutical Cocrystals: From Serendipity to Design to Application. *Drug Discovery Today* **2019**, *24*, 796−804.
(3) Bordignon, S.; Cerreia Vioglio, P.; Priola, E.; Voinovich, D.; Gobetto, R.; Nishiyama, Y.; Chierotti, M. R. Engineering Codrug Solid Forms: Mechanochemical Synthesis of an Indomethacin−Caffeine System. *Cryst. Growth Des.* **2017**, *17*, 5744−5752.
(4) Sathisaran, I.; Dalvi, S. Engineering Cocrystals of Poorly Water-Soluble Drugs to Enhance Dissolution in Aqueous Medium. *Pharmaceutics* **2018**, *10*, 108.
(5) Good, D. J.; Rodriguez-Hornedo, N. Solubility Advantage of Pharmaceutical Cocrystals. *Cryst. Growth Des.* **2009**, *9*, 2252−2264.
(6) Elder, D. P.; Holm, R.; Diego, H. L. de. Use of Pharmaceutical Salts and Cocrystals to Address the Issue of Poor Solubility. *Int. J. Pharm.* **2013**, *453*, 88−100.
(7) Schultheiss, N.; Newman, A. Pharmaceutical Cocrystals and Their Physicochemical Properties. *Cryst. Growth Des.* **2009**, *9*, 2950−2967.
(8) Kumar, A.; Kumar, S.; Nanda, A. A Review about Regulatory Status and Recent Patents of Pharmaceutical Co-Crystals. *Adv. Pharm. Bull.* **2018**, *8*, 355−363.
(9) Berry, D. J.; Steed, J. W. Pharmaceutical Cocrystals, Salts and Multicomponent Systems; Intermolecular Interactions and Property Based Design. *Adv. Drug Delivery Rev.* **2017**, *117*, 3−24.
(10) Grothe, E.; Meekes, H.; Vlieg, E.; ter Horst, J. H.; de Gelder, R. Solvates, Salts, and Cocrystals: A Proposal for a Feasible Classification System. *Cryst. Growth Des.* **2016**, *16*, 3237−3243.
(11) Aitipamula, S.; Banerjee, R.; Bansal, A. K.; Biradha, K.; Cheney, M. L.; Choudhury, A. R.; Desiraju, G. R.; Dikundwar, A. G.; Dubey, R.; Duggirala, N.; et al. Polymorphs, Salts, and Cocrystals: What's in a Name? *Cryst. Growth Des.* **2012**, *12*, 2147−2152.
(12) Aakeröy, C. B.; Fasulo, M. E.; Desper, J. Cocrystal or Salt: Does It Really Matter? *Mol. Pharmaceutics* **2007**, *4*, 317−322.
(13) Kelley, S. P.; Narita, A.; Holbrey, J. D.; Green, K. D.; Reichert, W. M.; Rogers, R. D. Understanding the Effects of Ionicity in Salts, Solvates, Co-Crystals, Ionic Co-Crystals, and Ionic Liquids, Rather than Nomenclature, Is Critical to Understanding Their Behavior. *Cryst. Growth Des.* **2013**, *13*, 965−975.
(14) Hathwar, V. R.; Pal, R.; Guru Row, T. N. Charge Density Analysis of Crystals of Nicotinamide with Salicylic Acid and Oxalic Acid: An Insight into the Salt to Cocrystal Continuum. *Cryst. Growth Des.* **2010**, *10*, 3306−3310.
(15) Wiechert, D.; Mootz, D. Molecular Beside Ionic: Crystal Structures of a 1/1 and a 1/4 Adduct of Pyridine and Formic Acid. *Angew. Chem., Int. Ed.* **1999**, *38*, 1974−1976.

DOI: 10.1021/acs.cgd.9b01299
Cryst. Growth Des. 2020, 20, 906−915

(16) Steiner, T.; Majerz, I.; Wilson, C. C. First O-H-N Hydrogen Bond with a Centered Proton Obtained by Thermally Induced Proton Migration. *Angew. Chem., Int. Ed.* **2001**, *40*, 2651−2654.
(17) Losev, E. A.; Boldyreva, E. V. A Salt or a Co-Crystal − When Crystallization Protocol Matters. *CrystEngComm* **2018**, *20*, 2299−2305.
(18) Perumalla, S. R.; Wang, C.; Guo, Y.; Shi, L.; Sun, C. C. Robust Bulk Preparation and Characterization of Sulfamethazine and Saccharine Salt and Cocrystal Polymorphs. *CrystEngComm* **2019**, *21*, 2089−2096.
(19) Stainton, P.; Grecu, T.; McCabe, J.; Munshi, T.; Nauha, E.; Scowen, I. J.; Blagden, N. First Comparative Study of the Three Polymorphs of Bis(Isonicotinamide) Citric Acid Cocrystals and the Concomitant Salt 4-Carbamoylpyridinium Citrate Isonicotinamide. *Cryst. Growth Des.* **2018**, *18*, 4150−4159.
(20) Jones, C. L.; Skelton, J. M.; Parker, S. C.; Raithby, P. R.; Walsh, A.; Wilson, C. C.; Thomas, L. H. Living in the Salt-Cocrystal Continuum: Indecisive Organic Complexes with Thermochromic Behaviour. *CrystEngComm* **2019**, *21*, 1626−1634.
(21) Zaman, K. Tuberculosis: A Global Health Problem. *J. Health Popul. Nutr.* **2010**, *28*, 111−113.
(22) Wang, F.; Langley, R.; Gulten, G.; Dover, L. G.; Besra, G. S.; Jacobs, W. R.; Sacchettini, J. C. Mechanism of Thioamide Drug Action against Tuberculosis and Leprosy. *J. Exp. Med.* **2007**, *204*, 73−78.
(23) Bastos, M. L.; Hussain, H.; Weyer, K.; Garcia-Garcia, L.; Leimane, V.; Leung, C. C.; Narita, M.; Penã, J. M.; Ponce-de-Leon, A.; Seung, K. J.; et al. Treatment Outcomes of Patients with Multidrug-Resistant and Extensively Drug-Resistant Tuberculosis According to Drug Susceptibility Testing to First- and Second-Line Drugs: An Individual Patient Data Meta-Analysis. *Clin. Infect. Dis.* **2014**, *59*, 1364−1374.
(24) *Ethionamide*; DrugBank, https://www.drugbank.ca/drugs/DB00609.
(25) Mannava, M. K. C.; Suresh, K.; Nangia, A. Enhanced Bioavailability in the Oxalate Salt of the Anti-Tuberculosis Drug Ethionamide. *Cryst. Growth Des.* **2016**, *16*, 1591−1598.
(26) Diniz, L. F.; Carvalho, P. S.; de Melo, C. C.; Ellena, J. Development of a Salt Drug with Improved Solubility: Ethionamide Nitrate. *J. Mol. Struct.* **2017**, *1137*, 119−125.
(27) Alléaume, M.; Leroy, F.; Gadret, M.; Goursolle, M. Structure Cristalline de Composés Antituberculeux. IV. Structure Cristalline de l'éthyl-2-Thiocarbamoyl-4 Pyridine. *Acta Crystallogr., Sect. B: Struct. Crystallogr. Cryst. Chem.* **1973**, *29*, 1994−2000.
(28) de Melo, C. C.; da Silva, C. C. P.; Pereira, C. C. S. S.; Rosa, P. C. P.; Ellena, J. Mechanochemistry Applied to Reformulation and Scale-up Production of Ethionamide: Salt Selection and Solubility Enhancement. *Eur. J. Pharm. Sci.* **2016**, *81*, 149−156.
(29) Aakeröy, C. B.; Beatty, A. M.; Helfrich, B. A. A High-Yielding Supramolecular Reaction. *J. Am. Chem. Soc.* **2002**, *124*, 14425−14432.
(30) Aakeröy, C. B.; Beatty, A. M.; Helfrich, B. A. Total Synthesis" Supramolecular Style: Design and Hydrogen-Bond-Directed Assembly of Ternary Supermolecules. *Angew. Chem., Int. Ed.* **2001**, *40*, 3240−3242.
(31) Spinelli, F.; Dichiarante, E.; Curzi, M.; Giaffreda, S. L.; Chierotti, M. R.; Gobetto, R.; Rossi, F.; Chelazzi, L.; Braga, D.; Grepioni, F. Molecular Salts of the Antidepressant Venlafaxine: An Effective Route to Solubility Properties Modifications. *Cryst. Growth Des.* **2017**, *17*, 4270−4279.
(32) Surov, A. O.; Vasilev, N. A.; Churakov, A. V.; Stroh, J.; Emmerling, F.; Perlovich, G. L. Solid Forms of Ciprofloxacin Salicylate: Polymorphism, Formation Pathways, and Thermodynamic Stability. *Cryst. Growth Des.* **2019**, *19*, 2979−2990.
(33) Duong, N. T.; Rossi, F.; Makrinich, M.; Goldbourt, A.; Chierotti, M. R.; Gobetto, R.; Nishiyama, Y. Accurate ^{1}H-^{14}N Distance Measurements by Phase-Modulated RESPDOR at Ultra-Fast MAS. *J. Magn. Reson.* **2019**, *308*, 106559.
(34) Nimerovsky, E.; Gupta, R.; Yehl, J.; Li, M.; Polenova, T.; Goldbourt, A. Phase-Modulated LA-REDOR: A Robust, Accurate and Efficient Solid-State NMR Technique for Distance Measurements between a Spin-1/2 and a Quadrupole Spin. *J. Magn. Reson.* **2014**, *244*, 107−113.
(35) *CrysAlis PRO*, v1.171.38.46; Rigaku Oxford Diffraction, 2015.
(36) Sheldrick, G. M. A Short History of SHELX. *Acta Crystallogr., Sect. A: Found. Crystallogr.* **2008**, *64*, 112−122.
(37) Sheldrick, G. M. Crystal Structure Refinement WithSHELXL. *Acta Crystallogr., Sect. C: Struct. Chem.* **2015**, *71*, 3−8.
(38) Bennett, A. E.; Rienstra, C. M.; Auger, M.; Lakshmi, K. V.; Griffin, R. G. Heteronuclear Decoupling in Rotating Solids. *J. Chem. Phys.* **1995**, *103*, 6951−6958.
(39) Fung, B. M.; Khitrin, A. K.; Ermolaev, K. An Improved Broadband Decoupling Sequence for Liquid Crystals and Solids. *J. Magn. Reson.* **2000**, *142*, 97−101.
(40) Giannozzi, P.; Baroni, S.; Bonini, N.; Calandra, M.; Car, R.; Cavazzoni, C.; Ceresoli, D.; Chiarotti, G. L.; Cococcioni, M.; Dabo, I.; et al. QUANTUM ESPRESSO: A Modular and Open-Source Software Project for Quantum Simulations of Materials. *J. Phys.: Condens. Matter* **2009**, *21*, 395502.
(41) Giannozzi, P.; Andreussi, O.; Brumme, T.; Bunau, O.; Buongiorno Nardelli, M.; Calandra, M.; Car, R.; Cavazzoni, C.; Ceresoli, D.; Cococcioni, M.; et al. Advanced Capabilities for Materials Modelling with Quantum ESPRESSO. *J. Phys.: Condens. Matter* **2017**, *29*, 465901.
(42) Dion, M.; Rydberg, H.; Schröder, E.; Langreth, D. C.; Lundqvist, B. I. Van Der Waals Density Functional for General Geometries. *Phys. Rev. Lett.* **2004**, *92*, 246401.
(43) Lee, K.; Murray, É. D.; Kong, L.; Lundqvist, B. I.; Langreth, D. C. Higher-Accuracy van der Waals Density Functional. *Phys. Rev. B: Condens. Matter Mater. Phys.* **2010**, *82*, 081101.
(44) Thonhauser, T.; Zuluaga, S.; Arter, C. A.; Berland, K.; Schröder, E.; Hyldgaard, P. Spin Signature of Nonlocal Correlation Binding in Metal-Organic Frameworks. *Phys. Rev. Lett.* **2015**, *115*, 136402.
(45) Thonhauser, T.; Cooper, V. R.; Li, S.; Puzder, A.; Hyldgaard, P.; Langreth, D. C. Van Der Waals Density Functional: Self-Consistent Potential and the Nature of the van Der Waals Bond. *Phys. Rev. B: Condens. Matter Mater. Phys.* **2007**, *76*, 125112.
(46) Berland, K.; Cooper, V. R.; Lee, K.; Schröder, E.; Thonhauser, T.; Hyldgaard, P.; Lundqvist, B. I. Van Der Waals Forces in Density Functional Theory: A Review of the VdW-DF Method. *Rep. Prog. Phys.* **2015**, *78*, 066501.
(47) Langreth, D. C.; Lundqvist, B. I.; Chakarova-Käck, S. D.; Cooper, V. R.; Dion, M.; Hyldgaard, P.; Kelkkanen, A.; Kleis, J.; Kong, L.; Li, S.; et al. A Density Functional for Sparse Matter. *J. Phys.: Condens. Matter* **2009**, *21*, 084203.
(48) Sabatini, R.; Küçükbenli, E.; Kolb, B.; Thonhauser, T.; de Gironcoli, S. Structural Evolution of Amino Acid Crystals under Stress from a Non-Empirical Density Functional. *J. Phys.: Condens. Matter* **2012**, *24*, 424209.
(49) Hamada, I. van der Waals Density Functional Made Accurate. *Phys. Rev. B: Condens. Matter Mater. Phys.* **2014**, *89*, 121103.
(50) Dal Corso, A. Pseudopotentials Periodic Table: From H to Pu. *Comput. Mater. Sci.* **2014**, *95*, 337−350.
(51) Monkhorst, H. J.; Pack, J. D. Special Points for Brillouin-Zone Integrations. *Phys. Rev. B* **1976**, *13*, 5188−5192.
(52) Franco, F.; Baricco, M.; Chierotti, M. R.; Gobetto, R.; Nervi, C. Coupling Solid-State NMR with GIPAW Ab Initio Calculations in Metal Hydrides and Borohydrides. *J. Phys. Chem. C* **2013**, *117*, 9991−9998.
(53) Pickard, C. J.; Mauri, F. All-Electron Magnetic Response with Pseudopotentials: NMR Chemical Shifts. *Phys. Rev. B: Condens. Matter Mater. Phys.* **2001**, *63*, 245101.
(54) Harris, R. K.; Hodgkinson, P.; Pickard, C. J.; Yates, J. R.; Zorin, V. Chemical Shift Computations on a Crystallographic Basis: Some Reflections and Comments. *Magn. Reson. Chem.* **2007**, *45* (S1), S174−S186.
(55) Reddy, G. N. M.; Cook, D. S.; Iuga, D.; Walton, R. I.; Marsh, A.; Brown, S. P. An NMR Crystallography Study of the Hemihydrate

DOI: 10.1021/acs.cgd.9b01299
Cryst. Growth Des. 2020, 20, 906−915

of 2′, 3′-O-Isopropylidineguanosine. *Solid State Nucl. Magn. Reson.* **2015**, *65*, 41−48.
(56) Chow, S. F.; Shi, L.; Ng, W. W.; Leung, K. H. Y.; Nagapudi, K.; Sun, C. C.; Chow, A. H. L. Kinetic Entrapment of a Hidden Curcumin Cocrystal with Phloroglucinol. *Cryst. Growth Des.* **2014**, *14*, 5079−5089.
(57) Kitamura, M. Strategy for Control of Crystallization of Polymorphs. *CrystEngComm* **2009**, *11*, 949−964.
(58) Cardew, P. T.; Davey, R. J. The Ostwald Ratio, Kinetic Phase Diagrams, and Polymorph Maps. *Cryst. Growth Des.* **2019**, *19*, 5798−5810.
(59) Schmidt, M. U.; Brüning, J.; Glinnemann, J.; Hützler, M. W.; Mörschel, P.; Ivashevskaya, S. N.; van de Streek, J.; Braga, D.; Maini, L.; Chierotti, M.; Gobetto, R. The thermodynamically stable form of solid barbituric acid: the enol tautomer. *Angew. Chem., Int. Ed.* **2011**, *50*, 7924−7926.
(60) Stolar, T.; Lukin, S.; Tireli, M.; Sovic, I.; Karadeniz, B.; Kerekovic, I.; Matijasič, G.; Gretic, M.; Katancič, Z.; Dejanovic, I.; di Michiel, M.; Halasz, I.; Uzarevic, K. Control of Pharmaceutical Cocrystal Polymorphism on Various Scales by Mechanochemistry: Transfer from the Laboratory Batch to the Large-Scale Extrusion Processing. *ACS Sustainable Chem. Eng.* **2019**, *7*, 7102−7110.
(61) Kaneniwa, N.; Otsuka, M. Effect of Grinding on the Transformations of Polymorphs of Chloramphenicol Palmitate. *Chem. Pharm. Bull.* **1985**, *33*, 1660−1668.
(62) Hasa, D.; Schneider Rauber, G.; Voinovich, D.; Jones, W. Cocrystal Formation via Mechanochemistry: from Neat and Liquid-Assisted Grinding to Polymer-Assisted Grinding. *Angew. Chem., Int. Ed.* **2015**, *54*, 7371−7375.
(63) Fischer, F.; Scholz, G.; Benemann, S.; Rademann, K.; Emmerling, F. Evaluation of the formation pathways of cocrystal polymorphs in liquid-assisted syntheses. *CrystEngComm* **2014**, *16*, 8272−8278.
(64) Hasa, D.; Miniussi, E.; Jones, W. Mechanochemical Synthesis of Multicomponent Crystals: One Liquid for One Polymorph? A Myth to Dispel. *Cryst. Growth Des.* **2016**, *16*, 4582−4588.
(65) Bhogala, B. R.; Basavoju, S.; Nangia, A. Tape and Layer Structures in Cocrystals of Some Di- and Tricarboxylic Acids with 4,4′-Bipyridines and Isonicotinamide. From Binary to Ternary Cocrystals. *CrystEngComm* **2005**, *7*, 551−562.
(66) Cruz-Cabeza, A. J. Acid−Base Crystalline Complexes and the PKa Rule. *CrystEngComm* **2012**, *14*, 6362−6365.
(67) Childs, S. L.; Stahly, G. P.; Park, A. The Salt−Cocrystal Continuum: The Influence of Crystal Structure on Ionization State. *Mol. Pharmaceutics* **2007**, *4* (3), 323−338.
(68) Kavanagh, O. N.; Walker, G.; Lusi, M. Graph-Set Analysis Helps To Understand Charge Transfer in a Novel Ionic Cocrystal When the ΔpK_a Rule Fails. *Cryst. Growth Des.* **2019**, *19*, 5308−5313.
(69) Chierotti, M. R.; Gobetto, R. Solid-State NMR Studies of Weak Interactions in Supramolecular Systems. *Chem. Commun.* **2008**, *14*, 1621−1634.
(70) Aitipamula, S.; Wong, A. B. H.; Chow, P. S.; Tan, R. B. H. Polymorphism and Phase Transformations of a Cocrystal of Nicotinamide and Pimelic Acid. *CrystEngComm* **2012**, *14*, 8193.
(71) Cavanagh, K. L.; Maheshwari, C.; Rodríguez-Hornedo, N. Understanding the Differences Between Cocrystal and Salt Aqueous Solubilities. *J. Pharm. Sci.* **2018**, *107*, 113−120.
(72) Chadha, R.; Saini, A.; Khullar, S.; Jain, D. S.; Mandal, S. K.; Guru Row, T. N. Crystal Structures and Physicochemical Properties of Four New Lamotrigine Multicomponent Forms. *Cryst. Growth Des.* **2013**, *13*, 858−870.
(73) Bolla, G.; Sanphui, P.; Nangia, A. Solubility Advantage of Tenoxicam Phenolic Cocrystals Compared to Salts. *Cryst. Growth Des.* **2013**, *13*, 1988−2003.
(74) Mittapalli, S.; Mannava, M. K. C.; Khandavilli, U. B. R.; Allu, S.; Nangia, A. Soluble Salts and Cocrystals of Clotrimazole. *Cryst. Growth Des.* **2015**, *15*, 2493−2504.
(75) Sandhu, B.; Sinha, A. S.; Desper, J.; Aakeröy, C. B. Modulating the Physical Properties of Solid Forms of Urea Using Co-Crystallization Technology. *Chem. Commun.* **2018**, *54*, 4657−4660.
(76) *Beta-Alanine*; DrugBank, https://www.drugbank.ca/drugs/DB03107.
(77) Variankaval, N.; Wenslow, R.; Murry, J.; Hartman, R.; Helmy, R.; Kwong, E.; Clas, D.; Dalton, C.; Santos, I. Preparation and Solid-State Characterization of Nonstoichiometric Cocrystals of a Phosphodiesterase-IV Inhibitor And l-Tartaric Acid. *Cryst. Growth Des.* **2006**, *6*, 690−700.
(78) *Marvin*, v19.22; ChemAxon, 2019; http://www.chemaxon.com).

DOI: 10.1021/acs.cgd.9b01299
Cryst. Growth Des. 2020, 20, 906−915